Radar backscattering changes in Arctic sea ice from late summer to early autumn observed by space-borne X-band HH-polarization SAR

Jeong-Won Park, Hyun-Cheol Kim, Sang-Hoon Hong, Sung-Ho Kang, Hans C. Graber, Byongjun Hwang & Craig M. Lee

Published online: 06 Apr 2016.

Submit your article to this journal 🖉

View related articles 🔍

View Crossmark data

Taylor & Francis
Taylor & Francis Group

Radar backscattering changes in Arctic sea ice from late summer to early autumn observed by space-borne X-band HH-polarization SAR

Jeong-Won Park[a,c], Hyun-Cheol Kim[a], Sang-Hoon Hong[a], Sung-Ho Kang[b], Hans C. Graber[d], Byongjun Hwang[e] and Craig M. Lee[f]

[a]Department of Polar Remote Sensing, Korea Polar Research Institute, Incheon, Korea; [b]Division of Polar Ocean Environment, Korea Polar Research Institute, Incheon, Korea; [c]Nansen Environmental and Remote Sensing Center, Bergen, Norway; [d]Center for Southeastern Tropical Advanced Remote Sensing, University of Miami, FL, US; [e]Scottish Marine Institute, Oban, Argyll, UK; [f]Applied Physics Laboratory, University of Washington, Seattle, WA, USA

ABSTRACT

Melt ponds are believed to play an important role in sea ice dynamics because they accelerate the melting of sea ice in the warmer spring and summer months. Additionally, they are known to absorb solar radiation rather than reflect it as the surrounding sea ice does. However, the size and distribution of melt ponds are highly variable, and thus, the contribution of melt ponds to sea ice melting should differ based on the maturity of the melt pond. Because of the harsh conditions of the Arctic, estimating the actual surface changes via *in situ* measurements and/or optical remote sensing data is difficult. In this study, we present a high-resolution time-series analysis of the short-term variation of sea ice and melt ponds over the Beaufort Sea using space-borne multispectral and synthetic aperture radar (SAR) images. A KOMPSAT-3 (Korea Multi-Purpose Satellite-3) optical image was used for an initial classification of the surface types, and 15 TerraSAR-X SAR images covering 46 days in the 2014 Arctic summer were used to perform a dense time-series analysis. The surface of the target sea ice was classified into six categories based on spectral characteristics. The temporal variation of the radar backscattering coefficient in each class exhibited a distinct pattern, which was closely related to surface changes. Overall, changes in the radar backscattering coefficient indicated dynamic surface changes, except over pressure ridges. All ice classes showed a two-step decrease in radar backscattering, whereas snow-covered ice surfaces exhibited far fewer changes compared to bare ice surfaces. The surfaces adjacent to ponds showed stronger negative decreases than other classes. The changes in dark melt pond classes presented a complex non-linear decrease, which differed from the stepwise decrease of blue melt ponds. These observations can be used for important modelling studies of surface melting/freezing rates and to infer the variation over large areas using remote sensing data.

CONTACT Hyun-Cheol Kim ✉ kimhc@kopri.re.kr 🖃 Department of Polar Remote Sensing, Korea Polar Research Institute, 26 Songdomirae-ro, Yeonsu-gu, Incheon 21990, Korea

1. Introduction

The Arctic sea ice is thinning at a dramatic rate, even faster than researchers previously expected (Stroeve et al. 2012). The recent reduction in Arctic sea ice coverage during the summer season is believed to have contributed to and resulted from global warming. Although the total volume of Arctic sea ice is very small compared to other ices in the ocean because of its thickness (IPCC 2013), its surface coverage is crucial to maintain Earth's net radiation balance. The main controlling factor of the surface melting rate is the surface melt pond fraction, which is explained by the ice-albedo feedback mechanism (Curry et al. 1995): A larger melt pond reduces the albedo, a lower albedo causes more melting, and more melting increases the pond fraction. One recent study (Schröder et al. 2014) reported that a strong correlation exists between the spring pond fraction and the September sea ice extent. In summer, melt ponds can cover 30–50% of first-year ice and 15–25% of multi-year ice (Fetterer and Untersteiner 1998). In general, first-year ice surfaces have large networks of connected shallow ponds, whereas the ponds in multi-year ice surfaces are deep and isolated (Eicken et al. 2004). The melt pond coverage has been measured in several Arctic regions via field surveys (Grenfell and Maykut 1977; Yackel, Barber, and Hanesiak 2000; Polashenski, Perovich, and Courville 2012), aerial photography (Derksen, Piwowar, and LeDrew 1997; Perovich, Tucker, and Ligett 2002; Birnbaum et al. 2009), and satellite imagery (Yackel and Barber 2000; Tschudi, Maslanik, and Perovich 2008; Rösel, Kaleschke, and Birnbaum 2012; Kim et al. 2013). Field observations provide the most precise melt pond properties, but it is impossible to investigate vast areas during short ice camp periods. There are also many areas inaccessible for direct measurement because of the difficulties research vessels may encounter in attempting to reach such places. Only remote sensing can provide more extensive mapping capabilities on a regular basis. Previous studies using satellite remote sensing mainly focused on the extraction of the surface melt pond fraction, particularly using multispectral sensors, such as Landsat (Markus, Cavalieri, and Ivanoff 2002; Rösel and Kaleschke 2011) and the Moderate Resolution Imaging Spectroradiometer (MODIS) (Rösel, Kaleschke, and Birnbaum 2012). The MODIS-based study demonstrated the most successful mapping capabilities for pan-Arctic sea ice. However, frequent cloud cover of up to 81% over Arctic seas hinders mapping with optical sensors (Schweiger 2004). In contrast, it is possible to collect dense time-series data sets using synthetic aperture radar (SAR) because of its day/night acquisition and ability to penetrate through cloud cover.

This study aimed to answer the following questions: It is possible to relate the melt pond extent to the surface change rate using high-resolution satellite data? If so, how will melt ponds affect the radar backscattering of various types of surface sea ice? To address these questions, we collected both multispectral and SAR images acquired from the Beaufort Sea (Figure 1) during the summer of 2014. As a part of a research collaboration between the Korea Polar Research Institute (KOPRI) and the marginal ice zone programme (Lee et al. 2012) of the U.S. Office of Naval Research (ONR), many satellite observations were requested and collected over the regions near Cluster 5. This study presents high-resolution dense time-series observations of sea ice surface changes from high-resolution space-borne imaging data. We hypothesized that the SAR back-scattering properties of the sea ice surface change as the melting/freezing process progresses and that the rate of change differs by surface type, which can be delineated clearly in high-resolution images.
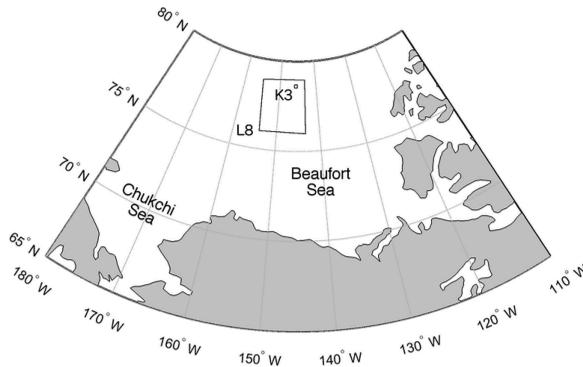
Figure 1. The coverage of optical images overlaid on a map of the study area. The large rectangle L8 and the small rectangle K3 represent the coverage of the Landsat-8 and KOMPSAT-3 (Korea Multi-Purpose Satellite-3) image, respectively. The coverage of the TerraSAR-X images was omitted to avoid visual complexity because they were acquired in 15 different footprints.

2. Methods

In this study, we used two types of high-resolution space-borne remote sensing data: multi-spectral optical data from KOMPSAT-3 and Landsat-8 and SAR data from TerraSAR-X. The basic characteristics of these data are summarized in Table 1. To relate the surface coverage and the rate of change, a dense time-series data set was utilized. The image-acquisition mechanisms of the optical and SAR sensors are very different, and thus, they sense the surface materials from different perspectives. In the case of sea ice and melt ponds, multispectral optical sensors can discriminate surface types based on spectral response patterns from multiple channels. Additionally, melt ponds can be subdivided into several types using spectral signatures (i.e., blue ponds, blue-green ponds, and dark ponds, as in Tschudi, Maslanik, and Perovich 2008). The colour of a melt pond depends on the thickness of the sea ice beneath the pond. In general, ponds over multi-year ice appear blue because their bottoms are less transparent, whereas ponds over first-year ice appear much darker (Divine et al. 2015). In SAR sensors, the backscattering intensities are strongly influenced by the surface roughness, the dielectric constant of the scatterers, and the orientation of the features (Sandven and Johannessen 2006). Additionally, the melt water distribution contributes to the dynamic backscattering signatures of the sea ice surface, but a radar signal cannot penetrate into the water surface, making it difficult to discriminate pond classes using a single-channel SAR image. Because the observation periods (mid-August–early October) include both late melting and early freeze-up phases, the backscattering signatures will reflect these changes in the time-series data.

To take full advantages of the two different sensors, the basic strategy was to combine the analytical results from each sensor. Figure 2 demonstrates the data-

Table 1. Specifications of the sensors and data used in this study.

Satellite name	Sensor type	Band	Acquisition date	Number of scenes	Spatial resolution
Landsat-8	Multispectral (MS)	11 channels in VNIR-TIR (0.43–2.3, 10.6–12.5 μm)	17 August 2014	1	30 m (MS) 15 m (PAN)
KOMPSAT-3	Multispectral (MS)	5 channels in VNIR (0.45–0.90 μm)	14 August 2014	1	2.8 m (MS) 0.7 m (PAN)
TerraSAR-X	Synthetic Aperture Radar (SAR)	1 channel in X-band (9.65 GHz), HH polarization	19 August–3 October 2014	15	3 m

MS: multispectral band; VNIR: visible and near infrared; PAN: panchromatic band; TIR: thermal infrared.
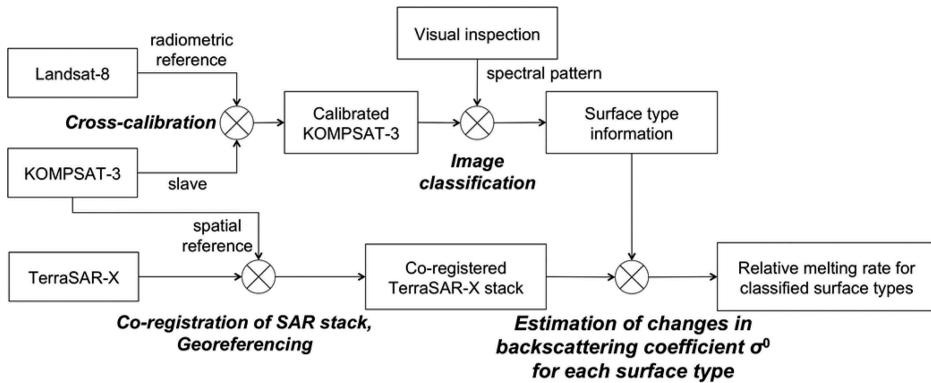
Figure 2. Data-processing workflow of this study.

processing workflow used in this study, which is described in this section. The main point is that optical and SAR data are used separately to perform an initial surface type classification and a time series analysis, respectively. Through this approach, we extracted distinctive radar backscattering changes over the different observation periods. The detailed methods used follow, and the results are discussed in the next section.

2.1. *Target ice floe selection*

In a time-series analysis of the same target, the target ice floe should be large enough to cover a large number of samples (pixels) in the image domain. Additionally, its structure should be solid enough to not experience deformation during the observation period. Based on these considerations, we selected a multi-year ice floe with a diameter of 3 km. During the observation periods, this ice floe drifted 147.8 km, and the mean centre location was at 77.46°N 143.38°W, near the southern ice margin of the Beaufort Sea.

2.2. *Cross-calibration of KOMPSAT-3 and Landsat-8 images*

The calibration coefficients of KOMPSAT-3 (Kim et al. 2015) have not been fully validated over polar oceans, where two radiometrically extreme features coexist: water and snow/ice. To convert the digital numbers (DN) into reflectance, we adopted a Landsat-8 Operational Land Imager (OLI) image as a cross-calibration source. Although the observation dates of the two sensors differed by 3 days, the two images were acquired in a very similar nadir-viewing geometry with almost the same spectral band selection in the visible and near infrared (VNIR) channels. To match the spectral characteristics of KOMPSAT-3 to those of Landsat-8, we first subsampled the KOMPSAT-3 image (2.8-m resolution) into the pixel spacing of Landsat-8 (30 m) using pixel aggregation. Then, we transformed the resampled KOMPSAT-3 image into the Landsat-8 geometry via a rigid body transform so that the two images had nearly identical contents. Unlike land-observation scenarios, the 3-day time gap does not allow for perfect one-to-one registration because of the motion and deformation of sea ice. However, the overall contents of the KOMPSAT-3 image (15 km by 15 km) are almost the same over such a short period. Because perfect co-registration is not guaranteed in this case, a least-squares fit of each pixel value would result in a biased estimation. We computed histograms of the KOMPSAT-3 DN values and corresponding Landsat-8 reflectance for each channel. Because the contents of two images were almost the same (Figure 3, upper row), their distributions were similar. A generalized extreme value distribution was used to fit each distribution, and the resulting gains (scale factor, *G*) and offsets (shifting factor, *O*) were calculated as follows:
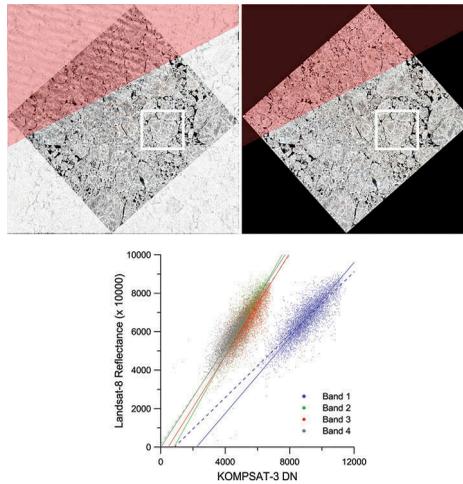
$$G = \sigma_{L8}/\sigma_{K3} \tag{1}$$

Figure 3. (Upper) Landsat-8 (left) and KOMPSAT-3 (right) images used for radiometric cross calibration. An area out of the common coverage was masked out with a bright tone, and the red polygon indicates the area with thin cloud cover where the pixels were excluded in the calibration process. The target ice floe is located in the centre of the white box. (Bottom) Scatter plot of the digital values of KOMPSAT-3 DN and Landsat-8 reflectance. Solid lines represent the regression lines computed by applying gains and offsets, while dashed lines represent those of direct least-squares fit.

$$O = \mu_{L8} - \mu_{K3}, \tag{2}$$

where σ and μ are the scale and location parameters of the model distribution, and subscripts L8 and K3 represent Landsat-8 and KOMPSAT-3, respectively. Finally, we obtained the calibrated KOMPSAT-3 image in its native full resolution by applying computed scale factors (G_1, G_2, G_3, and G_4) and shifting values (O_1, O_2, O_3, and O_4) to the original DN value of each band (subscripts represent the band number. Note that, we used four bands in VNIR).

2.3. Surface type classification of sea ice

As the main aim of this study was to identify the relationship between surface types and the corresponding changes during the observation period, we first divided the surface types into six classes according to the difference in their spectral albedos, following Grenfell and Maykut (1977): pressure ridges, white (snow-covered/dry) sea ice, grey (bare/melting) sea ice, blue melt ponds, dark melt ponds, and open water. Because there are four KOMPSAT-3 spectral bands, which are fewer than the number of classes, these data were insufficient to establish a large number of classes using unsupervised classification methods. We first selected 1000 pixels in each class by comparing the spectral similarity with those of six reference surface types; then, 70% of them were used as a training set, and the other 30% were used for verification. Although several algorithms can be used for supervised classification, we selected the minimum distance classification algorithm because it assumes that spectral variability is same in all directions; hence, there are no overlapping classes.

2.4. Generation of radar time series

To analyse the temporal variation of an ice floe, 15 TerraSAR-X images were acquired over acquisition dates from 19 August 2014 to 3 October 2014. The imaging mode was stripmap, which has an approximately 3 m spatial resolution. The absolute radiometric stability of TerraSAR-X data is known to be less than 0.2 dB (Schmidt et al. 2014). Because all of the delivered TerraSAR-X products are calibrated to radar brightness, β^0, we first converted them to normalized radar backscattering coefficient, σ^0, to enable inter-comparison of the

time-series data. Although the conversion process required knowledge of the local incidence angle over the whole illuminated area, no such *in situ* measurement was available. Therefore, we used ellipsoidal Earth geometry (WGS84) to compute the local incidence angle and then removed the incidence angle-dependent backscattering variance from the data themselves. The reference variance was estimated by applying a second-order polynomial fit to the data acquired over a relatively short period (24–28 September) with four different incidence angles (21.5°, 35.4°, 42.9°, and 55.1°). To reduce the inherent intensity fluctuations from speckle noise, a filtering process using NL-SAR (Deledalle et al. 2015) was adopted prior to geo-referencing. NL-SAR is a state-of-art non-local-based denoising filter, which introduces a patch similarity criterion and a weighted maximum likelihood estimation for noisy images with adapted weights derived from patches in a search window. We applied the NL-SAR filter to every SAR image with a half-search window size of 12, half-patch size of 5, and number of looks of 4. Because the time-series data were acquired from many different orbital paths and at various incidence angles, they first needed to be geo-referenced using state vectors and an Earth ellipsoidal model. Then, all of the other images were co-registered with the master image, which was acquired on the earliest date in the time-series data, to compensate for relative motion. Note that, there was no significant deformation in the target ice floe, and thus, we used a linear conformal transformation for the co-registration, which only incorporated the translation and rotation effects. Finally, we estimated the backscattering intensity changes for each pixel of the time-series data and compared them with the classification results deduced from the multispectral optical data.

3. Results and discussion

To achieve a high-resolution classification of sea ice surface types, we first cross-calibrated high-resolution KOMPSAT-3 images using a radiometrically stable Landsat-8 image. The bottom of Figure 3 shows a scatter plot relating the VNIR channels of KOMPSAT-3 and Landsat-8. The regression lines were computed by applying gains and offsets (solid line) and show strong agreement with the scatter distributions in Figure 3. A direct least-squares fit (dashed line) was not suitable because of the misregistration induced by ice motion between the two observation dates. Then, a minimum distance classification algorithm was applied to the calibrated KOMPSAT-3 image (Figure 4(b)). The confusion matrix in Table 2 validates the classification results with an overall accuracy of 93.9%. Note that, although the classification in this study might not be sufficient to reflect the true nature of Arctic sea ice, it included the most common classes. Furthermore, the number of classes that can be identified by a single polarization SAR image was also limited. After generating the radar time-series data, the (spatial) mean backscattering coefficients for each class were used to investigate the surface changes in each time-series data set. Because the backscattering coefficient can be altered by small differences in surface conditions, even within the same class, we used the class mean value for our analysis to suppress such effects. Note that, the temporal mean backscattering coefficient image (Figure 4(c)) is similar to the visual band image (Figure 4(a)): areas with a high pond fraction have low values of both the optical reflectance and radar backscattering. However, this positive correlation was not maintained throughout the whole observation period.

Figure 5 demonstrates the changes in the mean backscattering intensity over a 46-day observation period. The observation period included 17 September, which was the date of minimum Arctic sea ice extent in 2014 (NSIDC 2014). The wind speed and air temperature were also measured by an automatic weather station (AWS), which was installed approximately 4.5 km away from the target ice floe; these data also indicated
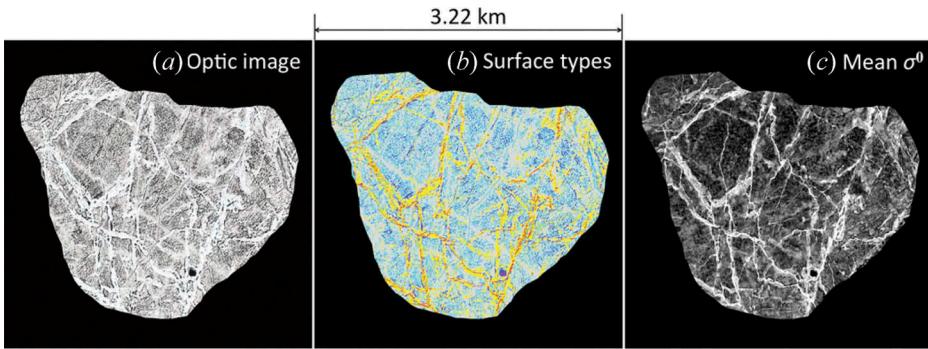
Figure 4. Target ice floe analysed in this study. (a) Red-green-blue (RGB) composite optical image; (b) Five surface class types: pressure ridge (red), white ice (yellow), grey ice (white), blue melt pond (cyan), and dark melt pond (purple); and (c) Temporal mean of radar backscattering coefficient (σ^0). Brighter tones correspond to higher backscatterings.

Table 2. Confusion matrix of the minimum distance classification results (Unit = %).

Classified data	Pressure ridge	White sea ice	Grey sea ice	Blue melt pond	Dark melt pond	Open water	User's accuracy
Pressure ridge	79.3	0	0	0	0	0	100
White sea ice	20.6	89.3	5.8	0	0	0	76.5
Grey sea ice	0.1	10.7	94.2	1.3	0	0	89.2
Blue melt pond	0	0	0	92.3	0.1	0	99.9
Dark melt pond	0	0	0	6.4	85.7	0.1	93.1
Open water	0	0	0	0	14.2	99.9	98.3
Producer's accuracy	79.3	89.3	94.2	92.3	85.7	99.9	–

Overall classification accuracy = 93.9%; Kappa coefficient = 0.91.

that the observation period included both late melting and early freezing periods. Because there was no *in situ* measurement available to confirm how the target's surface changed, we divided the observation periods into four categories, primarily based on air temperature. The boundary between the melt phase and intermediate phase was defined based on an abrupt decrease in the air temperature from approximately zero to sub-zero. Considering the atmospheric conditions and the peak of minimum sea ice extent of the year observed by passive microwave radar, the onset of the surface freeze-up occurred on approximately 13 September. The wind speed information suggested that the surfaces of the pond classes were not frozen in the intermediate phase because only the pond class exhibited notable changes in radar backscattering intensity, which reflected changes in the water surface roughness (Scharien and Yackel 2005). As the radar incidence angle varied from scene to scene in our dataset, the relationship between the wind speed and radar backscattering intensity was not necessarily positive in this case. Unfortunately, the AWS stopped working after 22 September; however, we divided the freeze-up phase into two phases by analysing the changes in the radar backscattering coefficients. Because the radar backscattering intensity changes mainly because of surface roughness, changes in backscattering indicate changes in the surface material's status. The backscattering intensity of the pressure ridge class remained almost constant, indicating that no significant external force was introduced and that the combined measurements from different orbital paths and incidence angles were reliable. The white ice class consists of typical multi-year ice with moderate topographic relief because both the optical albedo and radar backscattering exceeded those of the grey ice class. The backscattering intensity declined slightly during the late melting and
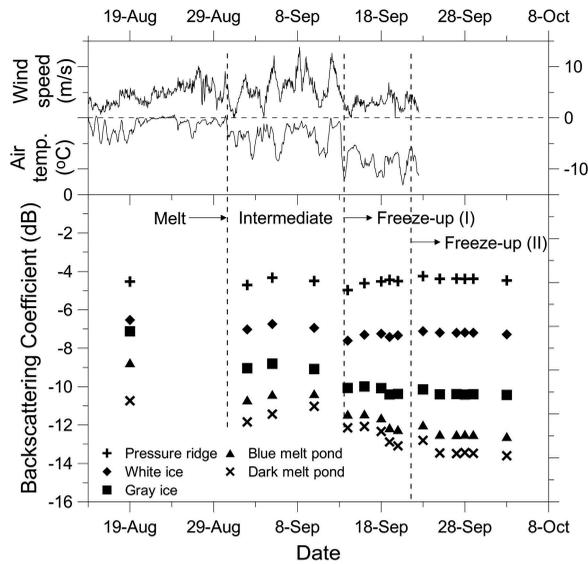
Figure 5. Changes in the class mean backscattering coefficient of TerraSAR-X observations between 19 August 2014 and 3 October 2014. The wind speed and air temperature were measured by an AWS. The observation period can be subdivided into four phases based on the change patterns.

intermediate phases but remained almost constant after the onset of freeze-up. The grey ice class, however, showed a clear two-step decrease throughout the whole observation period. Because the surface of the grey ice was very smooth and partly covered by remnant water overflowed from adjacent dark melt ponds and/or leads, the backscattering intensity declined during the melt season. After the melt season, the refrozen thin water layer further smoothed the surface, acting as specular scatterer and causing a second decrease in the radar backscattering (freeze-up phase I in Figure 5). After refreezing of the topmost layer, no further changes were observed.

The blue pond class was relatively small among the pond classes. Most were found on top of the white ice class, where the ice was thicker than in other areas. Their backscattering changes reflect rapid changes of the surface status. In the early part of our observation period, the backscattering intensity decreased by the end of August and then remained almost constant until the second decrease, which occurred during freeze-up phase I. The melting of small floating ice, which was a common feature in the blue melt ponds, might have induced the first rapid decrease. Subsequently, the surface refreeze caused a second, similar decrease, following the trend of the grey ice. The dark pond class had larger coverage than the blue pond class. The dark ponds were located within the interior part of the ice floe, surrounded by pressure ridges, where the topographic height is relatively low. Thus, the dark ponds started to melt earlier than the blue ponds and were mature, with less floating ice on the pond surface. As a result, they exhibited smaller backscattering decreases in the late melting phase and more backscattering fluctuations leading up to the early freeze-up phase. After the surface refroze, their change pattern was very similar to that of the blue ponds, with slightly lower values because of the presence of less surviving floating ice.

4. Conclusions

The sea ice surface changes related to melt ponds have been poorly evaluated using high-resolution space-borne remote sensing methods because continuous data acquisition over the Arctic sea is greatly constrained by weather conditions and the long revisit time. In this

study, we explored very high-resolution multispectral optical and SAR images to monitor sea ice surface changes, which are closely related to the surface coverage types. During the late summer to early autumn of 2014, we determined that the temporal variation of the radar backscattering coefficient in each class exhibited a distinct pattern, which was closely related to the surface changes. Overall, these changes in the backscattering coefficients indicated dynamic surface changes, except over pressure ridges. All of the ice classes exhibited a two-step decrease in radar backscattering, whereas snow-covered ice surfaces presented far fewer changes than bare ice surfaces. The surfaces adjacent to ponds had stronger negative changes in backscattering than those in other classes. The backscattering changes of the dark melt pond class exhibited a complex non-linear decrease, unlike the stepped decrease of the blue melt pond class. Although the classification of surface types using SAR data alone requires further investigation, our results clearly demonstrated that high-resolution SAR data can be effectively utilized to compute the surface melting/freezing rate and infer sea ice surface variations over large areas using remote sensing data.

Acknowledgements

Disclosure statement

Funding

References

Birnbaum, G., W. Dierking, J. Hartmann, C. Lüpkes, A. Ehrlich, T. Garbrecht, and M. Sellmann. 2009. "The Campaign MELTEX with Research Aircraft Polar 5 in the Arctic in 2008." *Reports on Polar and Marine Research* 593: 3–85.

Curry, J. A., J. L. Schramm, and E. E. Ebert. 1995. "Sea Ice-Albedo Climate Feedback Mechanism." *Journal of Climate* 8: 240–247. doi:10.1175/1520-0442(1995)008<0240:SIACFM>2.0.CO;2.

Deledalle, C.-A., L. Denis, F. Tupin, A. Reigber, and M. Jager. 2015. "NL-SAR: A Unified Nonlocal Framework for Resolution-Preserving (Pol)(In)Sar Denoising." *IEEE Transactions on Geoscience and Remote Sensing* 53 (4): 2021–2038. doi:10.1109/TGRS.2014.2352555.

Derksen, C., J. Piwowar, and E. LeDrew. 1997. "Sea-Ice Melt-Pond Fraction as Determined from Low Level Aerial Photographs." *Arctic and Alpine Research* 29 (3): 345–351. doi:10.2307/1552150.

Divine, D. V., M. A. Granskog, S. R. Hudson, C. A. Pedersen, T. I. Karlsen, S. A. Divina, A. H. H. Renner, and S. Gerland. 2015. "Regional Melt-Pond Fraction and Albedo of Thin Arctic First-Year Drift Ice in Late Summer." *The Cryosphere* 9: 255–268. doi:10.5194/tc-9-255-2015.

Eicken, H., T. C. Grenfell, D. K. Perovich, J. A. Richter-Menge, and K. Frey. 2004. "Hydraulic Controls of Summer Arctic Pack Ice Albedo." *Journal of Geophysical Research: Oceans* 109 (C8). doi:10.1029/2003JC001989.

Fetterer, F., and N. Untersteiner. 1998. "Observations of Melt Ponds on Arctic Sea Ice." *Journal of Geophysical Research: Oceans* 103 (C11): 24821–24835. doi:10.1029/98JC02034.

Grenfell, T., and G. Maykut. 1977. "The Optical Properties of Ice and Snow in the Arctic Basin." *Journal of Glaciology* 18: 445–463.

IPCC. 2013. *Climate Change 2013: The Physical Science Basis. Contribution of Working Group I to the Fifth Assessment Report of the Intergovernmental Panel on Climate Change.* Cambridge University Press, Cambridge1535 pp.

Kim, D.-J., B. Hwang, K. H. Chung, S. H. Lee, H.-S. Jung, and W. M. Moon. 2013. "Melt Pond Mapping with High Resolution SAR: The First View." *Proceedings of the IEEE* 101 (3): 748–758. doi:10.1109/JPROC.2012.2226411.

Kim, J., C. Jin, C. Choi, and H. Ahn. 2015. "Radiometric Characterization and Validation for the KOMPSAT-3 Sensor." *Remote Sensing Letters* 6 (7): 529–538. doi:10.1080/2150704X.2015.1054043.

Lee, C., S. Cole, M. Doble, L. Freitag, P. Hwang, S. Jayne, M. Jeffries, et al. 2012. "Marginal Ice Zone (MIZ) Program: Science and Experiment Plan." APL-UW TR 1201, Technical Report, Applied Physics Laboratory, University of Washington, Seattle, October 2012, 48 pp.

Markus, T., D. J. Cavalieri, and A. Ivanoff. 2002. "The Potential of Using Landsat 7 ETM+ for the Classification of Sea-Ice Surface Conditions during Summer." *Annals of Glaciology* 34 (1): 415–419. doi:10.3189/172756402781817536.

NSIDC (National Snow and Ice Data Center). 2014. "2014 Melt Season in Review." National Snow and Ice Data Center, October 7, 2014. Accessed October 23 2015. http://nsidc.org/arcticseaicenews/2014/10/

Perovich, D. K., W. B. Tucker III, and K. A. Ligett. 2002. "Aerial Observations of the Evolution of Ice Surface Conditions during Summer." *Journal of Geophysical Research* 107 (C10). doi:10.1029/2000JC000449.

Polashenski, C., D. Perovich, and Z. Courville. 2012. "The Mechanisms of Sea Ice Melt Pond Formation and Evolution." *Journal of Geophysical Research: Oceans* 117: C01001. doi:10.1029/2011JC007231.

Rösel, A., and L. Kaleschke. 2011. "Comparison of Different Retrieval Techniques for Melt Ponds on Arctic Sea Ice from Landsat and MODIS Satellite Data." *Annals of Glaciology* 52 (57): 185–191. doi:10.3189/172756411795931606.

Rösel, A., L. Kaleschke, and G. Birnbaum. 2012. "Melt Ponds on Arctic Sea Ice Determined from MODIS Satellite Data Using an Artificial Neural Network." *Journal of Geophysical Research: Oceans* 6 (2): 431–446. doi:10.5194/tc-6-431-2012.

Sandven, S., and O. M. Johannessen. 2006. "Sea Ice Monitoring by Remote Sensing." Chap. 8 in *Remote Sensing of the Marine Environment*, 241–283. In *Manual of Remote Sensing*, edited by J. Gower, 338 pp. 3rd ed. Vol. 6. Bethesda, MD: American Society for Photogrammetry and Remote Sensing.

Scharien, R. K., and J. J. Yackel. 2005. "Analysis of Surface Roughness and Morphology of First-Year Sea Ice Melt Ponds: Implications for Microwave Scattering." *IEEE Transactions on Geoscience and Remote Sensing* 43 (12): 2927–2939. doi:10.1109/TGRS.2005.857896.

Schmidt, K., G. C. Alfonzo, N. Tous-Ramon, M. Bachmann, and M. Schwerdt. 2014, "Calibration Performance of the Terrasar-X and Tandem-X Satellites since Launch." Proceedings of 10th European Conference on Synthetic Aperture Radar, Berlin, Germany, June 3–5.

Schröder, D., D. L. Feltham, D. Flocco, and M. Tsamados. 2014. "September Arctic Sea-Ice Minimum Predicted by Spring Melt-Pond Fraction." *Nature Climate Change* 4: 353–357. doi:10.1038/nclimate2203.

Schweiger, A. J. 2004. "Changes in Seasonal Cloud Cover over the Arctic Seas from Satellite and Surface Observations." *Geophysical Research Letters* 31 (12). doi:10.1029/2004GL020067.

Stroeve, J. C., M. C. Serreze, M. M. Holland, J. E. Kay, J. Malanik, and A. P. Barrett. 2012. "The Arctic's Rapidly Shrinking Sea Ice Cover: A Research Synthesis." *Climatic Change* 110 (3–4): 1005–1027. doi:10.1007/s10584-011-0101-1.

Tschudi, M. A., J. A. Maslanik, and D. K. Perovich. 2008. "Derivation of Melt Pond Coverage on Arctic Sea Ice Using MODIS Observations." *Remote Sensing of Environment* 112 (5): 2605–2614. doi:10.1016/j.rse.2007.12.009.

Yackel, J. J., and D. G. Barber. 2000. "Melt Ponds on Sea Ice in the Canadian Archipelago: 2. on the Use of RADARSAT-1 Synthetic Aperture Radar for Geophysical Inversion." *Journal of Geophysical Research: Oceans* 105 (C9): 22061–22070. doi:10.1029/2000JC900076.

Yackel, J. J., D. G. Barber, and J. M. Hanesiak. 2000. "Melt Ponds on Sea Ice in the Canadian Archipelago: 1. Variability in Morphological and Radiative Properties." *Journal of Geophysical Research: Oceans* 105 (C9): 22049–22060. doi:10.1029/2000JC900075.